Two-dimensional fatigue debonding in GFRP/balsa sandwich panels

Aida Cameselle-Molares, Anastasios P. Vassilopoulos, Thomas Keller[*]

Composite Construction Laboratory (CCLab), École Polytechnique Fédérale de Lausanne (EPFL), Station 16, Bâtiment BP, CH-1015 Lausanne, Switzerland

Abstract

An experimental investigation of the two-dimensional (2D) debonding behavior of GFRP/balsa sandwich panels with embedded circular disbonds at the face sheet/core interface subjected to out-of-plane fatigue loads was conducted. The constant amplitude fatigue experiments were performed under load control and different R-ratios. Two face sheet configurations were investigated: a pure woven ply layup (SPA) and a combination of continuous filament mat (CFM) and woven plies (SPB). For the latter, the CFM layers (which are prone to develop fiber-bridging) were placed above and below the woven plies. In contrast to one-dimensional (1D) beam-like fatigue fracture experiments, decreasing crack growth rates and stable crack propagation were achieved under load control as a result of the 2D growth of the disbonds. The fatigue fracture performance obtained under R=0.1 for the SPB configuration was less efficient than for the SPA configuration owing to the fiber-bridging crushing associated with high fatigue amplitudes. Under higher R-ratios, a reduced amount of fiber-bridging crushing was observed, leading to a corresponding crack arrest and much longer life. The load-displacement hysteresis loops exhibited an increase in the cyclic stiffness within each fatigue cycle throughout the experiments. This stiffening was mainly caused by in-plane stretching stresses that developed in the debonded part of the face sheets whose magnitude and evolution were evaluated based on the in-plane strains monitored during the experiments.

Keywords: 2D crack propagation; fatigue; composites; debonding; sandwich panels.

1. Introduction

The number of fiber-reinforced polymer (FRP) sandwich components in high-performance load-bearing structures has considerably increased in recent decades thanks to their numerous advantages such as high strength- and stiffness-to-weight ratios, rapid installation and versatility. Specifically, in the civil engineering domain, glass fiber-reinforced polymer (GFRP) sandwich bridge decks have been increasingly employed mainly due to their easy and rapid assembly and their great shape and thickness flexibility [1-6]. Among the different core materials typically used in sandwich bridge decks, balsa cores have proved to be an advantageous choice due to a sufficient shear capacity and the uniform support to the upper face sheet (in contact with traffic loads) that they provide [4-6].

---

[*] Corresponding author. Tel: +41216933226; e-mail: thomas.keller@epfl.ch

The load-bearing capacity of sandwich structural members can be compromised in the presence of disbonds between the face sheets and the core [7, 8]. Considering further that many structural components are subjected to both static and dynamic loads throughout their lifetime, accurate assessment of the debonding fracture behavior under both quasi-static and fatigue loading is essential for a reliable structural design. Since Mode I-dominated debonding is considered the most critical fracture mode in sandwich structures [8-10], particular emphasis has been placed on investigating debonding under tensile opening loads [7, 10-19]. The existence of disbonds in structural composite sandwich members under pure compression or bending may induce premature face sheet wrinkling causing the disbond to open and thus propagate mainly under Mode I. Furthermore, geometrical changes or curved geometries can also lead to significant out-of-plane tensile stresses. Most of the existing studies focus on debonding under quasi-static loading, while only limited investigations of debonding under fatigue loading can be found in the literature [20-25].

Both quasi-static and fatigue debonding fracture behaviors in sandwich members are currently investigated through beam-like one-dimensional (1D) specimens [20-33] where the disbond propagates in the longitudinal direction maintaining an approximately constant crack width (i.e. the width of the specimen). Of all the available and not yet standardized specimen configurations, the single cantilever beam (SCB) specimen has been reported as being the most appropriate for characterizing the face sheet/core opening fracture behavior [8-10, 34]. These 1D conditions are however not likely to be found in actual structural elements where the perimeter of embedded cracks may expand in all directions.

A more realistic fracture approach was studied in [35] where the two-dimensional (2D) delamination in GFRP plates with embedded circular pre-cracks subjected to out-of-plane quasi-static tensile loads was experimentally investigated. The results showed that a stiffening of the plates occurred, caused mainly by in-plane stretching stresses that developed in the opened parts of the laminates. The stretching occurred as a result of the boundary constraints inherent to a plate with an embedded crack. One of the studied plates was further numerically investigated in [36]. A 50% increase in the total strain energy released rate (SERR), compared to 1D double cantilever beam (DCB) fracture specimens with the same layup as the plates, was found. The increase in flexural stiffness (1D beams vs 2D plates) and above-mentioned stress stiffening resulted in an increase of the total amount of fiber-bridging developed, which caused the corresponding SERR increase.

The 2D fracture investigation was further extended to quasi-static 2D debonding in GFRP/balsa sandwich panels and presented in [37]. Circular embedded pre-cracks were introduced in the face sheet/core interfaces and subjected to out-of-plane tensile loads. Due to the in-plane stretching strain that, as expected, also developed in the debonded part of the face sheets, significant interlaminar shear

fracture modes (i.e. Mode II and III) were activated throughout the propagation of the cracks, causing crack migration and nucleation of new crack surfaces.

All the previously described 2D fracture investigations were carried out under quasi-static loading conditions, however, 2D effects are also expected under fatigue loading conditions. To the authors' knowledge, no investigations of the 2D fatigue fracture behavior of sandwich panels have yet been reported in the literature.

Thus, the main objective of this work was to experimentally investigate the fatigue 2D debonding behavior in GFRP/balsa sandwich panels and identify the differences compared to 1D fatigue fracture. The same sandwich panel configurations as for the quasi-static investigation [37] were selected for this study. The experimental set-up was also similar to that developed for the quasi-static experiments. Circular embedded disbonds were also introduced at the center of the face sheet/core interface and out-of-plane fatigue tensile loads were applied to open the crack. The experiments were performed under load control and under different R-ratios. The crack growth and temperature on the surface of the face sheet were constantly monitored throughout all the experiments. Load-displacement hysteresis loops were also recorded in all the experiments. Their shape, the different causes of the increase of their inner area and the global stiffness degradation were discussed. Additionally, considering the results reported in [35-37], in-plane stretching of the opened part of the face sheet was also expected. In order to quantify the developed stretching, the in-plane strains in the top surface of the face sheets were also monitored throughout the experiments.

2. Experimental program

2.1. Material description

Two types of glass fiber reinforcement were used to fabricate the face sheets of the investigated sandwich panels: a 390-g/m^2 woven fabric (W) with the same proportion of reinforcement in the warp/weft directions (i.e. 50/50) and a 600-g/m^2 long continuous filament mat (CFM). The former was supplied by Swiss-Composite (Switzerland) and the latter by Owens Corning (United States). For the matrix, an epoxy resin (Sicomin SR8100) appropriate for vacuum infusion production was selected. The material properties of the resin and the glass fibers of each reinforcement are reported in Table 1 (manufacturer data [38-40]). Regarding the core, commercial BALTEK® VCB balsa wood (supplied by Colevo, Switzerland) was used. The average density of the provided balsa blocks was 228.40 kg/m^3.

2.2. Specimen description

Two different configurations of the GFRP face sheet were investigated. The first configuration (designated SPA) consisted of 18 plies of woven reinforcement (i.e. W$_{18}$) and the second (SPB) of a symmetric layup combining nine plies of woven fabrics and two plies of CFM above and below (i.e.

$CFM_2/W_9/CFM_2$). The same configurations were experimentally investigated under quasi-static loading in [37]. The face sheet layups were selected so that they had comparable axial and flexural stiffnesses (see also [37]) and to avoid bending-extension coupling effects (i.e. they were symmetric). The same balsa core dimensions were used in all panels (see Table 2). A total of four panels, one pair of each configuration, were fabricated. The vacuum infusion technique was used to fabricate all the panels. The panels were cured under vacuum for at least 12 hours at room temperature and post-cured, also under vacuum, for eight hours at 45°C. The description and dimensions of each sandwich panel configuration are presented in Table 2. To differentiate static and fatigue experiments, an additional "F" is used in the panel denomination for the latter (e.g. SPA.1 for the first static and SPA.1F for the first fatigue panel).

A circular pre-crack of 60-mm diameter was introduced at the center of the face sheet/core interface using a 13-µm thickness Teflon film. The load to open and propagate the pre-crack was applied by means of a 30-mm head and 10-mm shank screw. The layout of the sandwich panels (top and side views) is shown in Fig. 1. As can be observed, the face sheets were anchored on the lateral sides to the balsa core to assure that no other crack distant from the pre-crack was created. The loading regions (i.e. the center of the panels where the screw is located) of all panels were reinforced with three additional circular 60-mm diameter layers of woven reinforcement. Further details regarding the fabrication and assembling process can be found in [37].

2.3. Experimental set-up, loading and instrumentation

The tensile load was applied by a 100-kN MTS Landmark servo-hydraulic experimental rig with a load cell of 25 kN calibrated to 20% of its maximum capacity at a temperature of 22±3°C and relative humidity of 40±5%. The experimental set-up is presented in Fig. 2. The bottom of the panels was fixed and constrained to the bottom grip of the machine and the loading screw was then tightened to the surface of the panels with a nut, washer and rubber ring to distribute the pressures (Fig. 1). Finally, an in-house-developed hinge was placed between the loading screw and the upper grip to prevent any potential damage of the loading cell of the machine as a result of any small rotation of the screw. A level was used to guarantee the horizontality of the panels with respect to the vertical loading line. Initially, a quasi-static loading ramp was performed under displacement control at a rate of 1.5 mm/min until the mean fatigue load was achieved. Subsequently, the load control fatigue loading was initiated. This procedure was followed in all the experiments. The cyclic loading was performed initially and up to two million cycles at a frequency of 5 Hz. Subsequently, and until the end of the experiments, the frequency was increased to 10 Hz. The load and opening displacement were obtained from the machine (accuracy of ±0.5%) throughout the experiments. High acquisition frequencies were initially applied, recording load-displacement measurements at every cycle, followed by a progressive reduction. After two million cycles (i.e. at 10 Hz of fatigue loading), measurements were only recorded at every one million cycles.

The data acquisition capability of the machine permitted a total of 20 load and displacement measurements per cycle at 5 Hz and 10 measurements/cycle at 10 Hz.

A total of five fatigue experiments were conducted on the four fabricated sandwich panels. A summary of the performed experiments is presented in Table 3. As can be seen, experiments under the same R-ratio of $R=0.1$ were conducted on each of the two SPA panels (i.e. SPA.1F and SPA.2F). Regarding the SPB panels, and in order to evaluate the effect of the R-ratio on the fiber-bridging developed in SPB panels (which was expected to be dense based on the quasi-static results), three different R-ratios were investigated: $R=0.1$, applied to one of the panels (SPB.1F), and $R=0.5$ and 0.3, both applied consecutively to the second panel due to the limited fatigue crack propagation exhibited under the first condition. After the first experiment at $R=0.5$, the panel was unloaded. Subsequently, the initial quasi-static ramp to reach the mean fatigue load corresponding to $R=0.3$ was applied. The two experiments were designated SPB.2F1 and SPB.2F2 respectively (see Table 3). All experiments were performed until failure or until 12.5 million cycles which corresponded to a service life of 100 years for a bridge on main roads with low flow rates of lorries (see traffic category 3 in [41]).

The maximum fatigue loads were assigned based on the quasi-static results obtained for the same type of panels in [37]. Continuously increasing quasi-static loads were obtained throughout the experiments up to a maximum value, after which they decreased. These maximum values were considered as the characteristic [42] fracture resistance (P_k) of the investigated sandwich panels. Thus, in order to evaluate the fatigue performance of the two configurations, their respective design fatigue resistance values (P_d), calculated at ultimate limit state (ULS) level according to Eurocomp EUR 27666 [42], were used to calculate the maximum fatigue loads (P_{max}) using Eq. 1:

$$P_{max} = \frac{P_d}{\gamma_{Ff}} = \frac{\overline{P_k}}{\gamma_{mf} \cdot \gamma_{Ff}} = \frac{\overline{P_k}}{\gamma_{m,1} \cdot \gamma_{m,2} \cdot \gamma_{m,3} \cdot \gamma_{m,4} \cdot \gamma_{Ff}} \tag{1}$$

where $\overline{P_k}$ is the average of the maximum registered quasi-static loads (see [37]), γ_{mf} is the partial safety factor for material and γ_{Ff} is the partial safety factor for fatigue actions ($\gamma_{Ff} = 1.0$ unless agreed otherwise [42]). As indicated in Eq. 1, four partial coefficients ($\gamma_{m1,2,3,4}$) are comprised in γ_{mf}. Each takes into account different effects of material properties. These effects, and the corresponding coefficient's values applicable to the investigated sandwich panels, are summarized in Table 4. Likewise, the calculated and applied maximum fatigue loads (P_{max}), together with the load amplitudes (ΔP), are indicated in Table 3 for both configurations. The R-ratios were applied maintaining a constant value of the P_{max}.

The 2D crack propagation was monitored using two different systems: a digital camera and 3D Digital Image Correlation (DIC) system. A total of six rulers with markers every 2.5 mm were drawn on the surface of each panel, as can be observed in Fig. 3. The crack propagation along these rulers was

monitored by the digital camera located above the panels (see Fig. 2). At the beginning of the experiments, images were taken every two seconds (i.e. acquisition frequency of 0.5 Hz). As the crack propagation rate decreased, the acquisition frequency was likewise progressively decreased. The target area was permanently illuminated with a non-heating LED EFFILUX bar of white light (Fig. 2). The crack front was identified by the whitening of the delaminated areas recognizable thanks to the translucency of the face sheet laminates. The 3D DIC system (also located above the panels, see Fig. 2) was used to measure the out-of-plane deformation and in-plane strain distributions (accuracy of ±0.005 mm and ±0.01% respectively) of the top surface of one quarter of the face sheets (see Fig. 3). A random speckle pattern was applied on the measuring surface by means of white paint and black spray paint. The changes from straight to curved in the out-of-plane deformation profiles were assumed as being the crack front. The 3D DIC cameras had a maximum acquisition rate of 100 images/s. Therefore, a maximum of 20 images/cycle were recorded for each of the measured cycles at 5-Hz fatigue loading. Correspondingly, 10 images/cycles were recorded at 10 Hz. The cycle acquisition frequency was also varied throughout the experiments. During the first cycles, images were taken each 100 cycles and the frequency then progressively increased. From two million cycles and until the end of the experiments, images were taken every 50000 cycles. The DIC measuring area was also illuminated with a non-heating LED EFFILUX white light. The post-processing of the results was carried out using Vic-3D software from Correlated Solutions Inc. [43].

To verify whether the increase in the fatigue frequency from 5 to 10 Hz triggered a significant temperature increase at the crack front, the evolution of the temperature at the surface of the face sheets was monitored with an infrared (IR) thermal camera (accuracy of ±0.1°C) which was also located above the panels as can be seen in Fig. 2. In order to have a reference surface where the temperature was not affected by the fatigue opening and crack growth, a piece of GFRP laminate isolated from the face sheets by means of hard rubber was glued to the outer part of the panels (see Fig. 2). The image acquisition protocol was similar to that previously described for the digital camera.

3. Experimental results

3.1. Crack growth and displacement responses in SPA panels

The fatigue crack growth results, measured throughout the experiments on the SPA configuration (two different panels under R=0.1, see Table 3), are presented in Fig. 4. Since (as expected based on the quasi-static results in [37]) the cracks propagated concentrically (see Fig. 3), crack values are indicated as total radial crack lengths (i.e. with the 30-mm radius of the pre-crack included).

The cracks increased rapidly at the beginning of the two experiments, the growth rate then progressively decreased and finally approached a plateau after four million cycles. Almost identical total radial crack lengths were obtained and, although the exhibited plateaus differed slightly, similar mean values of total

6

radial crack lengths were achieved (118.7 mm and 118.3 mm for SPA.1F and SPA.2F respectively). Both experiments ended before reaching the serviceability number of cycles (i.e. 12.5 million) due to the failure in the loading region where, as a result of the local damage of the face sheet, the screw was pulled out. The SPA.2F panel sustained almost 60% more cycles than SPA.1F, see Table 3. Consequently, a longer plateau was exhibited in the latter case.

As the crack propagated, the opening displacement values, both maximum (δ_{max}) and minimum (δ_{min}), increased to maintain the target maximum and minimum fatigue loads. In Fig. 5 the consequently increasing displacement increment (i.e. δ_{max} - δ_{min}) responses of both panels are presented. As can be observed, similar behaviors were exhibited up to approximately one million cycles. Then, the curves started to differ, i.e. the SPA.2F panel exhibited lower values. However, approximately the same displacement value was achieved before failure (3.7 and 3.6 mm for SPA.1F and SPA.2F respectively). The common general trend (i.e. fast initial increase followed by a progressive deceleration) is in agreement with the previously described crack propagation behavior.

After a certain degree of crack propagation, the additional layers of reinforcement inserted over the face sheet laminate in the loading region (see Section 2.2) started to detach in both panels. The cycle interval corresponding to this detaching process (from initiation to complete detachment) is indicated as "RD" (reinforcement detachment) in Fig. 4 and Fig. 5. The initiation occurred at similar total radial crack lengths (90.0 mm in SPA.1F and 92.5 mm in SPA.2F) and after a similar number of cycles (~1 and ~1.2 million cycles respectively). The complete detachment of the layers occurred in both panels after the stabilization of the crack (i.e. already in the plateau region). However, the detachment process required more cycles in SPA.2F than in SPA.2F (~2.9 and ~6.8 million cycles respectively).

3.2. Crack growth and displacement responses in SPB configuration panels

The fatigue crack growth results corresponding to the experiments on the SPB configuration are presented in Fig. 6. As in the SPA panels, concentric crack propagation was obtained and thus crack values are also given in terms of total radial crack length. Depending on the selected *R*-ratio (see Table 3), very different fatigue behaviors were exhibited.

The crack in SPB.1F (*R*=0.1) propagated rapidly throughout the experiment, without exhibiting any significant reduction in crack growth rate. At 105 mm of total radial crack length the loading region failed and the screw was pulled out. This occurred after 1.09 million cycles and thus much earlier than in either of the two SPA panels which were also loaded at *R*=0.1 (see Section 3.1). Considering the short fatigue life shown for the SPB configuration at *R*=0.1, a smaller amplitude (*R*=0.5) was applied to the second panel (SPB.2F, Table 3). As can be observed in Fig. 6, a plateau in the total radial crack length was quickly approached after a short initial rapid crack growth during the first 10 mm of radial

propagation. Thus, almost no variation of the crack front was registered after approximately 1.5 million cycles. Furthermore, no noticeable damage occurred at the loading region. The experiment was stopped after the serviceability 12.5 million cycles were reached. In Table 3 the arrow indicates run-out specimens. Due to the reduced crack propagation (only 15 mm of radial increase) and the almost intact loading region after completing the SPB.2F1 experiment, a second experiment (i.e. SPB.2F2) under R=0.3 was performed on the same panel. At this intermediate amplitude, the crack increased at a fairly constant rate throughout the experiment (see Fig. 6). As for SPB.2F1, the experiment was stopped after the serviceability 12.5 million cycles were reached, which corresponded to a total radial crack length of 87.5 mm. More cycles would have been necessary to develop the plateau. Localized damage had already developed in the loading region.

The variation of the displacement increment during each of the three SPB experiments is shown in Fig. 7. The results are in agreement with the above-mentioned crack growth behavior, showing a steep increase for SPB.1F, barely varying for SPB.2F1 and steadily increasing for SPB.2F2.

The detachment of the reinforcement layers was only observed in SPB.1F and SPB.2F2 (see "RD" in Fig. 6 and Fig. 7). In the SPB.1F experiment it initiated after 57.5 mm of radial propagation (i.e. a total radial crack length of 87.5 mm) and ~0.7 million cycles. The complete detachment occurred simultaneously with the rapid local damage of the region. Regarding SPB.2F2, the detachment initiated at a total radial crack length of 72.5 mm and after ~8.5 million cycles.

3.3. Crack area growth rate

To better understand the described changes in the propagation rates, the fatigue crack area growth rate (i.e. dA/dN, henceforth referred to simply as "crack growth rate") vs the total crack area (i.e. with the pre-crack area included) curves are presented in Fig. 8. An incremental polynomial fitting, similar to that recommended for 1D specimens in ASTM E647-15e1 [44], was used to calculate the crack growth rate. According to this method, a second-order polynomial is fitted to groups of a specific number of successive data points (seven here). The slope of the fitted equation at any point corresponded to the crack growth rate.

As can be observed in Fig. 8, for all the experiments, the crack growth rate continuously decreased as the total crack area increased. Nevertheless, this decrease was not constant throughout the experiments, showing different behaviors depending on the experiment. Three regions could be identified for the two SPA experiments: 1) an initial region with a rapid decrease in the crack growth rate (from initiation to ~5000 mm^2 of total crack area); 2) an intermediate region exhibiting a moderate decrease in the crack growth rate and 3) a final region with again a rapid crack growth rate decrease (from ~40000 mm^2 of total crack area until the end of the experiments). The first region corresponded to the first 10 mm of

radial crack propagation in Fig. 4 and the last region to the exhibited plateau. Thus, the intermediate region corresponded to the major part of the fatigue experiments (see Fig. 4).

Regarding the SPB experiments, a strong effect of the R-ratio, as already evident in Fig. 6, was observed. The curve corresponding to R=0.1 (SPB.1F) only showed the first and second regions (in Fig. 8) due to the early failure of the panel (i.e. the plateau in Fig. 6 was not reached). The three regions were exhibited in SPB.2F1 (R=0.5) showing a rapid crack growth rate decrease from ~0.003 mm^2/cycle to ~0.002 mm^2/cycle (at the beginning of the experiment), followed by a more moderate decrease down to ~10^{-5} mm^2/cycle and again a rapid crack growth down to ~10^{-8} mm^2/cycle when the serviceability 12.5 million cycles were reached (after only 15 mm of radial propagation (see Fig. 6)). Finally, in the curve corresponding to R=0.3 (SPB.2F2) only the intermediate region was exhibited, showing that for this particular fatigue loading, the last region would have developed after more than 12.5 million cycles.

3.4. Load-displacement hysteresis loops and stiffness degradation

The load-displacement hysteresis loops developed during the fatigue loading of SPA.1F are presented in Fig. 9. The upper and lower parts of the loops corresponded respectively to the loading and unloading portions of the cycles. As can be observed, the loops exhibited a particular shape, referred to as "banana" shape in literature [45]. This shape became more accentuated as the crack propagated. The loops shifted towards the right as a result of the increase in the opening displacement. Furthermore, the area inside the loops (corresponding to the dissipated energy within a cycle) followed an increasing trend with the number of cycles, as can be observed for the two SPA panels in Fig. 10 (N_f is the total number of cycles sustained in the experiment). Similar behavior was obtained for all the experiments.

The global stiffness of the panels at each cycle, K, was assumed as being the slope of the hysteresis loops as defined in Fig. 9. The evolution of the global stiffness in all the experiments is presented in Fig. 11. A sharp initial degradation of the stiffness was exhibited in all panels. After a progressive decrease in the degradation rate, a plateau was achieved in SPA.1F, SPA.2F and SPB.2F1 experiments whereas in SPB.2F2, although a progressive decrease was also exhibited, the plateau did not completely develop. Again, similar behavior was exhibited in both SPA panels. In SPB.1F, only a small reduction occurred in the degradation rate before failure.

In Fig. 12, the crack growth rate is plotted against the global stiffness for all the experiments, showing a strong correlation between both parameters. The stabilization of the crack (i.e. no propagation) coincided with the stabilization of the global stiffness (i.e. no further degradation) for both SPA configuration experiments (once again showing comparable results) and for SPB.2F1, which showed the steepest curve. Neither the crack propagation nor the global stiffness stabilized however in SPB.1F and SPB.2F2 experiments.

The evolution of the global stiffness throughout all the experiments vs the total crack area is presented in Fig. 13. As can be observed, almost overlapping curves were obtained for all the configurations and R-ratios, confirming that the selected layups of the face sheets had, as intended, exhibited a comparable bending stiffness (see Section 2.2).

3.5. Radial and circumferential strain distribution

The in-plane radial and circumferential strains in the top surface of the face sheet were extracted from the 3D DIC measurements recorded during the experiments as described in Section 2.3. The strain profiles corresponding to a radial path (starting from the pre-crack front) in the SPA.1F panel are shown in Fig. 14. Three groups of profiles, corresponding to three different fatigue cycles, are presented: the black profiles, extracted at cycle 500,000; the orange profiles, extracted at cycle 1.0 million and the green profiles, extracted at cycle 1.5 million. The crack tip is indicated for each group of strain profiles (i.e. at a total radial crack length of 77.5, 95.0 and 105.0 mm respectively). The radial strain profiles were partially in compression and partially in tension while full tensile circumferential strain profiles were obtained. The typical compression state in the laminate in front of the crack tip ([46], i.e. in the un-cracked region) can be observed, mainly in the radial profiles.

3.6. Evolution of face sheet surface temperature

The distribution and magnitude of the surface temperature in four of the performed experiments, before the last fatigue cycles, are shown in Fig. 15. The presented temperature scale ranges from 10°C to 42°C. The regions exhibiting higher temperatures (i.e. hotspots outside the measuring scale) are thus indicated in white. Due to the comparable fatigue behavior obtained in both SPA.1F and SPA.2F experiments, a similar evolution of the surface temperature was obtained. Thus, only one of two SPA experiments (i.e. SPA.2F) is shown in Fig. 15. As can be observed, a clear hotspot (white color) was detected in the loading area for SPA.2F and SPB.1F due to the high internal friction generated owing to the concentrated damage in the region, which, ultimately, led to failure. Due to the absence of damage in the loading region of SPB.2F1 (*R*=0.5), no temperature increase occurred throughout the 12.5 million cycles. The intermediate loading case (R=0.3, SPB.2F2) already exhibited a temperature increase in the loading area after the serviceability 12.5 million cycles, which correlated with the already visible localized damage. The corresponding maximum temperatures registered in the loading region of the panels immediately before failure/end of the experiments are presented in Table 3. They remained well below the glass transition temperature of the laminate (66.3°C onset value from DMA) and thus did not cause any significant material softening.

No relevant temperature increase at the crack front (compared to the reference surface) was registered in any of the experiments (see dashed lines in Fig. 15). However, the temperature was measured on the

surface of the face sheets and therefore, if a temperature increase occurred around the crack tip, for instance, as a result of the friction of the developing fiber-bridging, the generated temperature may have dissipated through the thickness of the laminate.

4. Discussion

4.1. Load vs displacement control in 1D and 2D fatigue experiments

Quasi-static investigations of 2D delamination in laminated plates [35] and 2D debonding in sandwich panels [37] have proved that continuously increasing loads are required to propagate an embedded 2D crack due to the natural increase of the length of the perimeter of the 2D crack (i.e. the crack front) and the resulting disproportional growth of the crack area. This 2D behavior is the opposite of the typical 1D behavior of beam-like fracture experiments where cracks propagate with a constant crack front length under decreasing loads. As a result of this difference, the experimental fatigue fracture behavior under load and displacement control modes in 1D crack propagation cases is different from that in 2D cases. A comparison of these cases is discussed in the following.

The schematic quasi-static load-displacement curves corresponding to 1D and 2D crack propagation are presented in Fig. 16. These curves correspond to simplified fracture cases where after the critical load and opening displacement at which the crack is initiated (i.e. P_{cr}^{0} and δ_{cr}^{0} in Fig. 16) no relevant fracture process zone (FPZ) develops. The fatigue loading state after the propagation of a certain crack length "a" and a certain crack area "A" is evaluated considering both displacement and load control. Under displacement control, maintaining, for instance, δ_{cr}^{0} as the maximum fatigue opening displacement (δ_{max}), the maximum fatigue load corresponding to a crack length "a" (P_a) or crack area "A" (P_A) is smaller than the quasi-static critical load corresponding to the same crack length (P_{cr}^{a} and P_{cr}^{A} respectively). Consequently, a stable fatigue propagation of the crack, eventually reaching a non-propagating state indicating the absence of fatigue damage, is achieved under displacement control in both 1D and 2D fracture experiments. However, this is not the case when fatigue experiments are performed under load control. If, following the same reasoning as in displacement control, P_{cr}^{0} is selected as the maximum fatigue load (P_{max}), different results are obtained for 1D and 2D cases. In 1D cases, the selected P_{max} will always be greater, irrespective of the crack length, than the corresponding quasi-static critical load. As can be observed in Fig. 16(a), for the evaluated crack length "a", P_{max} is greater than P_{cr}^{a}. Therefore, an unstable crack propagation occurs under load control for 1D experiments if the static critical load is selected as the maximum fatigue load. To overcome this problem, in 1D fracture experiments under load control, a maximum fatigue load significantly smaller than the critical static load is typically selected, thus permitting an initial slow and stable propagation before the final rupture of the specimen (i.e. when the selected P_{max} reaches the corresponding P_{cr}^{a}). In the 2D case (Fig. 16(b)), and again selecting P_{cr}^{0} as the maximum fatigue load (P_{max}), the quasi-static critical load corresponding to a crack area "A" (P_{cr}^{A}) is always greater than P_{max}. It can therefore be concluded that,

owing to the continuously increasing load required to propagate a 2D crack, stable crack propagation can also be achieved under load control. This conclusion is corroborated by the 2D fatigue results presented in this investigation where, under load control, an initially fast crack propagation was registered followed by progressive stabilization.

As a result of the stable crack propagation always associated with displacement control in 1D fatigue experiments, they are easier to perform than those under load control. Thus, displacement control experiments are generally preferred in 1D fatigue investigations [33, 34]. As has been shown, in 2D crack propagation cases, both load and displacement control lead to a stable propagation of the crack and final crack arrest. However, as can be observed in Fig. 16(b), the amount of crack propagation under displacement control may be considerably smaller than that under load control due to the more drastic reduction of load at the crack tip associated with displacement control. This reduction in the amount of propagated crack may lead to incomplete development of the three regions (see Section 3.3.) associated with crack propagation under fatigue. Consequently, load-controlled experiments may even be preferable for 2D crack propagation investigations. Further experimental work is required to fully confirm this statement.

4.2. Effect of local damage in loading region

Throughout the experiments, the stiffness of the loading region of the panel face sheets was progressively reduced due to 1) the detachment of the reinforcement layers and 2) the local damage of the face sheet laminate. Any local stiffness reduction was however compensated by an increment in the already increasing opening displacement and thus did not affect the propagation of the investigated cracks. This was possible thanks to the load control conditions applied to all the experiments, which assured the continuous loading of the crack front.

For instance, as shown in Fig. 5, in both SPA panels a jump in the displacement was exhibited after the initiation of the detachment of the reinforcement layers (indicated as "RD", see Section 3.1) whereas the propagation of the crack continued. As the opening displacement increased, local damage progressively appeared in the loading region of the face sheet laminate, which reached failure after attaining the maximum displacement increment (i.e. around 3.7 mm for the SPA configuration panels, see Section 3.1). Due to the more rapid detaching process occurring in SPA.1F (see the length of "RD" region), the mentioned maximum displacement increment (and thus failure) was reached ~4.5 million cycles earlier than in SPA.2F (see Table 3). In view of the fact that the crack propagation was already stabilized before failure in both panels, no fatigue fracture data was lost. This can also be concluded from Fig. 8 where a sharp decrease of the crack growth rate was exhibited in both panels towards the end of the experiments.

Regarding the SPB.1F and SPB.2F2 experiments, the local stiffness reduction due to the detachment of the reinforcement layers was also compensated by the increased displacement. A jump was exhibited in

the displacement curve of the SPB.1F experiment whereas, as a result of the slow progression of the detachment process, a smoother variation in the displacement curve was observed in the SPB.2F2 experiment (see Fig. 7). In both cases, the propagation also continued until failure for SPB.1F and until the serviceability number of cycles for SPB.2F2.

The continuously decreasing trend of the global stiffness, K (extracted from the load-displacement hysteresis loops as described in Section 3.4), showed that a general softening of the panels occurred. Both crack propagation and K evolved similarly throughout the fatigue experiments (see Figs. 4, 6 and 11), eventually exhibiting a simultaneous stabilization. It can thus be concluded that the local progressive damage in the loading region did not affect the fracture behavior of the panels.

4.3. R-ratio effects

The fracture behavior of the investigated sandwich panel configurations under quasi-static opening loads [37] showed that, compared to the SPA panels, the introduction of CFM plies at the face sheet/core interface enhanced the load-bearing performance and led to a significant crack arrest in the SPB panels. The dense fiber-bridging generated during crack propagation was the cause of the improved fracture behavior. However, this conclusion cannot be directly applied to the fatigue fracture behavior, where, as discussed in the following, the fiber-bringing effect under fatigue loads was highly dependent on the selected R-ratio.

The two SPA configuration experiments and SPB.1F experiment were performed under the same R-ratio (i.e. R=0.1) and thus the obtained fatigue fracture behaviors are comparable. Based on the quasi-static behavior, a denser fiber-bridging was expected in the SPB configuration than in the SPA configuration, also resulting in a significant crack arrest and therefore steeper (again compared to SPA panels) dA/dN vs total crack area curves (Fig. 8). However, due to the high fatigue amplitudes (ΔP) associated with low R-ratios such as R=0.1, the cyclic crack closure in the SPB.1F experiment crushed most of the fibers-bridging the crack faces and any contribution of the fiber-bridging to the fracture performance was consequently minimized. As a result, as can be observed in Fig. 8, the SPB.1F panel exhibited a less steep dA/dN-total crack area curve than SPA panels which proved that, under R=0.1 fatigue loading, the SPB configuration did not result in a better fracture performance than the SPA configuration, as was the case under quasi-static loading conditions.

Comparing the results of the three SPB configuration experiments, the influence of the R-ratio can be clearly observed (Fig. 8). As discussed above, R=0.1 led to an almost complete destruction of the fiber-bridging and consequently, a rapid increase of the crack and opening displacement occurred within the first million cycles (see Fig. 6). As a result, the third branch of the dA/dN-total crack area curve, corresponding to the stabilization of the crack (see Section 3.3), was lacking. Steeper dA/dN-total crack

area curves were obtained for increasing R-ratios. Specifically, almost no crack propagation occurred under R=0.5, thus indicating a rapid crack arrest as a result of the dense non-destroyed fiber-bridging. As the experiment under R=0.3 (SPB.2F2) was performed on the same panel as the SPB.2F1 experiment, the fiber-bridging generated during the latter was already present and thus the first branch of the dA/dN-total crack area curve was lacking and yet an intermediate slope between R=0.1 and R=0.5 was exhibited. Similar effects of the R-ratio on fiber-bridging were reported in [27] (1D-experiments).

4.4. Load-displacement hysteresis loops and stretching-stiffening effect

The "banana" shape exhibited by the load-displacement hysteresis loops in all the performed experiments was caused by an increase of the cyclic stiffness (K^*) within each cycle. The slopes corresponding to the initial and last stiffnesses (K_0^* and K_1^* respectively) are indicated in Fig. 17(a) for the SPA.1F hysteresis loops corresponding to 0.6 and 3 million cycles. Additionally, the compliance (calculated as δ/P within a cycle) vs fatigue load curves corresponding to the loading part of both cycles are presented in Fig. 17(b). Typically, in 1D experiments, as a result of crack propagation, the compliance increases throughout the loading of the cycle [35]. However, as can be observed in Fig. 17(b), for the investigated 2D experiments, the compliance initially increased up to a maximum and subsequently decreased, thereby indicating an initial softening followed by a stiffening within the same cycle. Similarly to both quasi-static 2D panel delamination and 2D sandwich debonding [35, 37], the stiffening was caused mainly by the in-plane stretching (in both the radial and circumferential directions), due to the geometrical constraints, in the opened part of the laminate. Within each of the load cycles the stiffening occurred only after a certain level of deformation and thus after a certain increase of the load (i.e. the softening prevailed at the beginning of each cycle). As a result of the crack propagation and opening displacement increase, the deformation of the face sheet (and thus the in-plane stretching strains and stresses) also increased. The ratio between the initial and last cyclic stiffnesses (i.e. K_1^*/K_0^*, see Fig. 17) can be used to quantify the stiffening effect within each cycle. As expected, a smaller ratio was obtained at 0.6 million cycles (1.09, i.e. 9% increase) compared to 3 million cycles (1.28, i.e. 28% increase).

As mentioned in Section 3.4 and observed in Fig. 10 for the SPA panels, the area inside the loops exhibited an increasing trend with number of cycles for all the studied cases. Four sources of energy dissipation contributed to this increase: 1) the energy released as a result of the propagation of the main crack; 2) the energy released due to the damage created in the loading region; 3) the thermal energy dissipation at the crack tip as a result of the friction created in the fiber-bridging zone and 4) the thermal energy dissipation as a result of the friction between the crack faces generated in the loading region. The contribution of each of the sources varied throughout the experiments. Initially, during the rapid increase of the crack area, the energy released due to the propagation of the crack prevailed (see the rapid increase in the hysteresis area in Fig. 10). Subsequently, when the crack started to stabilize (i.e. approached the

plateau) and the damage in the loading region initiated, the damage and thermal energy dissipation in the loading region (i.e. sources 2 and 4) constituted the main source until the end of the experiments. Since the hysteresis area started approaching a plateau in this phase however, this latter contribution must have been significantly smaller than the former).

In beam-like specimens, small hysteresis areas develop and thus the hysteresis of the cyclic load-displacement behavior is typically disregarded (i.e. a linear behavior is assumed [47]). However, the length of the crack front increased throughout the propagation of an embedded 2D crack, resulting in a disproportional growth of the crack area [35, 37]. Consequently, considerably more energy (in terms of J, not J/m^2) is dissipated during the propagation of a 2D crack, thus increasing the hysteresis.

4.5. Derivation and evolution of in-plane stretching strains

If the face sheets of the investigated sandwich panels were under pure bending conditions, zero strain points corresponding to the change from compression to tension strains (such as those exhibited in the radial strain profiles presented in Fig. 14(a)) would necessarily indicate the location of an inflection point. However, the out-of-plane deflection radial profiles of the top surface of the face sheets (extracted from the DIC measurements) did not reveal an inflexion point at the exhibited zero strain points, as can be observed for the SPA.1F panels (particularly at 0.5 million cycles) in Fig. 18. This mismatch between inflection and zero strain points was attributed to the radial in-plane stretching strains which counteracted the bending compression strains and increased the bending tensile strains. The full tensile circumferential strains present in the top surface of the face sheet (see Fig. 14(b)) were increased by the corresponding in-plane circumferential stretching strains. Similar results were obtained for the quasi-static sandwich panels [37].

Using both the measured radial top strains and the curvature derived from the deflection profile, the corresponding radial bottom strains and stretching strains were derived. The stretching strains were subtracted from the total top and bottom strains to obtain the "pure" bending strain profiles. All the profiles are shown in Fig. 18(b)). A detailed description of this procedure can be found in [37]. The derived stretching values may not be accurate close to the fracture process zone (FPZ) since they are affected by the fiber-bridging. Further discussion regarding this effect can be found in [37]. As can be observed in the stretching strain profile, towards the extremes (i.e. loading region and crack tip) higher values were obtained as a result of the greater deformation exhibited in these regions. Linear "pure" bending strain profiles were also obtained, representing the linear behavior inherent to a punctual load.

The radial stretching strain profiles corresponding to the other two cycles represented in Fig. 14 (i.e. 1.0 and 1.5 million cycles) were likewise extracted and are shown, together with the profile at 0.5 million cycles, in Fig. 19. As can be observed, a general increasing trend (mainly from 0.5 million to 1 million

cycles) of the stretching strains occurred as the crack propagated and thus the face sheet deformed. This constitutes further confirmation of the increase of the stiffening effect obtained revealed in the load-displacement hysteresis loops and discussed in Section 4.4. For the sake of comparison, three radial stretching profiles corresponding to one of the SPA sandwich panels (SPA.2) quasi-statically investigated in [37] were added to Fig. 19. The total crack lengths corresponding to the evaluated fatigue cycles were similar to those corresponding to the quasi-static profiles. For the same total radial crack lengths, the corresponding quasi-static load was always higher than the maximum fatigue load investigated here. Consequently, the fatigue stretching strains were smaller than the quasi-static stretching strains.

4.6. Location and evolution of inflection points

The location of the inflection point was determined for different total radial crack lengths throughout the SPA.1F experiment. If the inflection point was located inside the DIC measuring area (i.e. from the pre-crack front onwards) it was already identified in the radial out-of-plane deflection profiles and if it was located outside the measuring area (i.e. in the pre-crack area) it could be identified by extending the pure bending linear profiles (see Fig. 18(b)).

The evolution of the inflexion point location with respect to the total radial crack length (i.e. L/a) for SPA.1F is presented in Fig. 20. For the sake of comparison, results corresponding to the quasi-static SPA.2 panel are also shown. Opposite behaviors were obtained under quasi-static and fatigue loading, exhibiting increasing and decreasing trends of L/a values respectively. As discussed in [37], the propagation of the crack shifted the inflection point towards the exterior of the face sheet (i.e. increasing L/a) while the local damage in the loading region shifted the inflection point towards the center of the face sheet (i.e. decreasing L/a). The effective location of the inflection point was thus the result of both opposing effects. In the quasi-static experiments, the propagation of the crack prevailed over the local damage of the loading region, shifting the inflection point towards the exterior of the face sheet. For the fatigue experiments on the other hand, the shift due to the local damage in the loading region prevailed over that of the propagation of the crack, moving the inflection point towards the center of the face sheet.

5. Conclusions

An experimental program designed to study the 2D fatigue face sheet debonding in GFRP/balsa sandwich panels with embedded cracks subjected to out-of-plane fatigue tensile loads was conducted. Two different face sheet configurations were investigated via a total of five experiments. One of the configurations (SPA) consisted of a pure woven fabric layup while in the other (SPB) layers of continuous filament mat were inserted above and below the woven plies. Circular pre-cracks were introduced at the face sheet/core interface. Experiments were performed under load control and under different R-ratios. The crack growth and opening displacement responses and the in-plane strain

distributions of the face sheet were examined. Likewise, the *R*-ratio effects, developed load-displacement hysteresis loops and evolution of the global stiffness were analyzed. Furthermore, the differences between displacement-control and load-control fatigue loading in 1D and 2D fracture experiments were thoroughly discussed. The following conclusions were drawn:

1. Decreasing crack growth rates were obtained under load-control fatigue conditions exhibiting a threefold trend: 1) an initial rapid decrease, 2) a moderate decrease and 3) a final rapid decrease. The first and third stages corresponded, respectively, to the initial rapid propagation of the crack and final arrest of crack propagation. Depending on the experiment, full or partial development of the described stages was achieved.

2. The decreasing crack growth rates obtained in the 2D fatigue experiments under load control are in contrast with those of standard 1D beam-like fatigue experiments under load control, where increasing crack growth rates (up to failure) are exhibited (i.e. an unstable crack propagation and final rupture of the specimen occur). This particular 2D fracture fatigue behavior was attributed to the increasing load required to propagate a 2D crack due to the constant increase of the crack front length (i.e. the perimeter of the 2D crack). As a result, the quasi-static load required to maintain the propagation of a 2D crack will always be greater than any selected maximum fatigue load and thus a stable propagation and final arrest of a 2D crack can always be achieved under load control conditions.

3. The fracture efficiency of including plies prone to develop fiber-bridging at the face sheet/core interface was found to be strongly dependent on the type of loading (i.e. quasi-static or fatigue) and, particularly under fatigue, on the considered *R*-ratio. Under quasi-static conditions, the introduction of such layers enhanced the fracture performance due to the dense fiber-bridging generated. However, due to the high fatigue amplitude associated with low *R*-ratios such as *R*=0.1, most of the fibers bridging the crack faces were broken, thus minimizing any fiber-bridging contribution and therefore not providing any improvement in terms of fatigue fracture performance. Increasing *R*-ratios however positively affected the fatigue performance due to the decrease in fiber-bridging crushing.

4. Due to the increasing length of the crack front throughout the propagation of an embedded 2D crack and the corresponding disproportional growth of the crack area, the amount of dissipated energy due to crack nucleation also increased as the crack propagated. As a result, the hysteresis area exhibited by the load-displacement loops considerably increased during the propagation of the crack. This behavior was the opposite of that of 1D beam-like specimens where the hysteresis of the cyclic load-displacement behavior is typically small and thus disregarded.

5. The load-displacement hysteresis loops exhibited an increase in the cyclic stiffness within each fatigue cycle. As in the quasi-static experiments, this stiffening was caused mainly by in-plane stretching stresses (developed as a result of the geometrical constraints). Based on the top surface face sheet in-plane strains extracted from the DIC measurements, the magnitude of the in-plane radial stretching strains was quantified showing an increasing trend of the in-plane stretching with increasing crack propagation. The magnitudes of load and displacement were smaller in the fatigue experiments than in the quasi-static experiments, resulting in a less deformed face sheet and thus smaller stretching strains.

Acknowledgments

References

1. Hollaway, L. A review of the present and future utilization of FRP composites in civil infrastructure with reference to their important in-service properties. Constr. Build. Mater., 2010; 24(12): 2419:2445.

2. Keller, T. Recent all-composite and hybrid fiber-reinforced polymer bridges and buildings. Prog. Struct. Eng. Mater., 2001; 3(2): 132-140.

3. Uddin, N. Developments in Fiber-Reinforced Polymer (FRP) Composites for Civil Engineering. 1st ed. Woodhead Publishing; 2013.

4. Keller, T., Rothe, J., De Castro, J., Osei-Antwi, M. GFRP-Balsa Sandwich Bridge Deck: Concept, Design, and Experimental Validation. J. Compos. Constr., 2013; 18(2): 04013043.

5. Osei-Antwi, M., De Castro, J., Vassilopoulos, A.P., Keller, T. Structural limits of FRP-balsa sandwich decks in bridge construction. Composites: Part B, 2014; 63: 77-84.

6. Osei-Antwi, M., De Castro, J., Vassilopoulos, A.P., Keller, T. FRP-Balsa Composite Sandwich Bridge Deck with Complex Core Assembly. J. Compos. Constr., 2013; 17(6): 04013011.

7. Cantwell, W.J., Davies, P. A test technique for assessing core-skin adhesion in composite sandwich structures. Journal of Material Science Letters, 1994; 13: 203-205.

8. Ratcliffe, J.G., Reeder, J.R. Sizing a single cantilever beam specimen for characterizing facesheet-core peel debonding in sandwich structure. Journal of Composite Materials, 2011; 45(25): 2669-2684.

9. Saseendran, V., Berggreen, C., Krueger, R. Mode mixity analysis of face/core debonds in a single cantilever beam sandwich specimen. J. Sandwich Structures and Materials, 2018; 0(0): 1-31.

10. Farmand-Ashtiani, E., Cugnoni, J., Botsis, J. Monitoring and characterization of the interfacial fracture in sandwich composites with embedded multiplexed optical sensors. Composite Structures, 2013; 96: 476-483.

11. Cantwell, W.J., Scudamore, R. Ratcliffe, J., Davies, P. Interfacial fracture in sandwich laminates. Comp. Sci. Tech., 1999; 54(14): 2079-2085.

12. Carlsson, L.A., Matteson, R.C., Aviles, F., Loup, D.C. Crack path in foam core DCB sandwich fracture specimens. Compos. Sci. Technol., 2005;65:2612-21.

13. Li, X., Carlsson, L.A. The tilted sandwich debond (TSD) specimen for face/core interface fracture characterization. J. Sandwich Structures and Materials, 1999; 1: 60-75.

14. Li, X., Carlsson, L.A. Elastic foundation analysis of tilted sandwich debond (TSD) specimen. J. Sandwich Structures and Materials, 2000; 2: 3-32.

15. Ratcliffe, J., Cantwell, W.J. A new test geometry for characterizing skin-core adhesion in thin-skinned sandwich structures. Journal of Material Science Letters, 2000; 19: 1365-1367.

16. Ural, A., Zehnder, A.T., Ingraffea, A.R. Fracture mechanics approach to facesheet delamination in honeycomb: measurement of energy release rate of adhesive bond. Eng Fract Mechs, 2003; 70: 93-103.

17. Shivakumar, K.N., Smith, S.A. in situ fracture toughness testing of core materials in sandwich panels. Journal of Composite Materials, 2004; 39(8): 655-668.

18. Berggreen, C., Simonsen, B.C., Borum, K.K. Experimental and numerical study of interface crack propagation in foam-cored sandwich beams. Journal of Composite Materials, 2007; 41(4): 493-520.

19. Stutz, S., Cugnoni, J., Botsis, J. Studies of mode I delamination in monotonic and fatigue loading using FBG wavelength multiplexing and numerical analysis. Compos. Sci. Technol., 2011; 71: 443-449.

20. Berkowitz, K.C., Johnson, W. Fracture and fatigue tests and analysis of composite sandwich structure. Journal of Composite Materials, 2004; 39(16); 1417-1431.

21. Shafiq, B., Quispitupa, A. Fatigue characteristics of foam core sandwich composites. International Journal of Fatigue, 2006; 28(2): 96-102.

22. Shipsha, A., Burman, M., Zenkert, D. Interfacial fatigue crack growth in foam core sandwich structures. Fatigue and Fracture of Engineering Materials and Structures, 1999; 22: 123-131.

23. Manca, M., Berggreen, C., Carlsson, L.A. G-control fatigue testing for cyclic crack propagation in composite structures. Eng. Frac. Mechs., 2015; 149: 375-386.

24. Gillespie, J.W., Carlsson, L.A., Gawandi, A.A., Bogetti, T.A. Fatigue crack growth at the face sheet-core interface in a discontinuous ceramic-tile cored sandwich structure. Composite Structures, 2012; 94: 3186-3193.

25. Manca, M., Quispitupa, A., Berggreen, C., Carlsson, L.A. Face/core debond fatigue crack growth characterization using the sandwich mixed mode bending specimen. Composites: Part A, 2012; 43: 2120-2127.

26. Shahverdi, M., Vassilopoulos, A.P., Keller, T. Experimental investigation of R-ratio effects on fatigue crack growth of adhesively-bonded pultruded GFRP DCB joints under CA loading. Composites Part A, 2012; 43(10); 1689-1697.

27. Bak, B.L.V., Sarrado, C., Turon, A., Costa, J. Delamination under fatigue loads in composite laminates. A review of the observed phenomenology and computational methods. Appl. Mech. Rev., 2014; 66: 060803-1-060803-24.

28. Rans, C., Alderliesten, R.C., Benedictus, R. Misinterpreting the results: how similitude can improve our understanding of fatigue delamination growth. Compos. Sci. Technol., 2011; 124: 214-227.

29. Simon, I., Banks-Sills, L., Fourman, V. Mode I delamination propagation and R-ratio effect in woven composite DCB specimens for a multi-directional layup. Inter. Journal of Fatigue, 2017; 96: 237-251.

30. Pascoe, J.A., Alderliesten, R.C., Benedictus, R. Towards understanding fatigue disbond growth via cyclic strain energy. Procedia Mater. Sci., 2014; 3: 610-615.

31. Brunner, A.J., Murphy, N., Pinter, G. Development of a standardized procedure for the characterization of interlaminar delamination propagation in advanced composites under fatigue mode I loading conditions. Eng. Frac. Mechs., 2009; 76: 2678-2689.

32. Campilho, R.D.S.G., da Silva, L.F.M. Mode I fatigue and fracture behavior of adhesively-bonded carbon fibre-reinforced polymer (CFRP) composite joints. Fatigue and Fracture of Adhesively-bonded Composite Joints: Ed. Vassilopoulos A.P. Woodhead Publishing; 2015.

33. Renart, J., Costa, J., Sarrado, C., Budhe, S., Turon, A., Rodríguez-Bellido, A. Mode I fatigue behavior and fracture of adhesively-bonded fibre-reinforced polymer (FRP) composite joints for structural repairs. Fatigue and Fracture of Adhesively-bonded Composite Joints: Ed. Vassilopoulos A.P. Woodhead Publishing; 2015.

34. Yoshida, K., Aoki, T. Beam on elastic foundation analysis of sandwich SCB specimen for debond fracture characterization. Composite Structures, 2018; 195: 83-92.

35. Cameselle-Molares A., Vassilopoulos A.P., Keller T. Experimental investigation of two-dimensional delamination in GFRP laminates. Eng. Frac. Mechs., 2018; 203: 152-171.

36. Cameselle-Molares A., Vassilopoulos A.P., Renart J., Turon A., Keller T. Numerical simulation of two-dimensional in-plane crack propagation in FRP laminates. Comp. Struc. 2018; 200: 396-407.

37. Cameselle-Molares A., Vassilopoulos A.P., Keller T. Two-dimensional quasi-static debonding in GFRP/balsa sandwich panels. Composite Structures, 2019; 215: 391-401.

38. Swiss Composite Product Catalogue. <https://www.swiss-composite.ch/pdf/Produkteuebersicht.pdf > (Accessed 16 October 2017).

39. Owen's Corning Reinforcements Composite Solutions Guide. <http://www.ocvreinforcements.com/pdf/library/Composite_Solutions_Guide_100360_E_finalprintable.pdf> (Accessed 26 March 2018).

40. Sicomin SR8100 resin datasheet. <http://www.sicomin.com/datasheets/product-pdf94.pdf> (Accessed 12 November 2018).

41. EN 1991-2 Eurocode 1. Actions on structures – Part 2: Traffic loads on bridges.

42. Clarke, J.L. (ed.). Structural design of polymer composites: Eurocomp design code and handbook. London: E & FN Spon; 1996.

43. Correlated Solutions Inc. VIC 3D-v7 reference manual. Columbia, USA: Correlated Solutions.

44. ASTM E647-15e1: Standard Test Method for Measurement of Fatigue Crack Growth Rates, ASTM International, West Conshohocken, PA, 2015.

45. Vieille, B., Albouy, W. About the applicability of a simple model to predict the fatigue life and behavior of woven-ply thermoplastic laminates at T>Tg. Composites Part B, 2014; 61: 181-190.

46. Pappas, G., Botsis, J. Intralaminar fracture of unidirectional carbon/epoxy composite: experimental results and numerical analysis. Int. J. Solids and Struc., 2016; 85-86: 114-124.

47. Pascoe, J.A., Alderliesten, R.C., Benedictus, R. On the relationship between disbond growth and the release of strain energy. Eng. Fract. Mechs., 2015; 133: 1-13.

Tables:

Table 1. Material properties: Young modulus (E), Shear modulus (G), Poisson ratio (v) and density (ρ)

Material	E (GPa)	G (GPa)	v (-)	ρ (g/cm³)
Epoxy resin	3.00	1.30	0.35	1.14
E-CR* glass (for CFM)	80.00	32.80	0.22	2.62
E-glass (for woven)	72.00	29.50	0.22	2.55

*CR: Corrosion-Resistant

Table 2. Description of GFRP/balsa sandwich panel configurations

Panel type	GFRP face laminate				Dimensions of Baltek® VBC balsa core (mm)
	Layout	Thickness t (mm)	Axial stiffness (GPa)	Bending stiffness (GPa)	
SPA	$(W)_{18}$	5	128.10	266.87	400 x 400 x 108
SPB	$(CFM)_2/(W)_9/(CFM)_2$	6	106.01	230.90	400 x 400 x 108

Table 3. Summary of fatigue experiments and results

Experiment	P_{max} (kN)	ΔP (kN)	R-ratio	Number of cycles (x10^6)	Temperature at last cycle (ºC)
SPA.1F	4.53	4.07	0.1	7.88 (failure)	54
SPA.2F				12.35 (failure)	59
SPB.1F		4.21	0.1	1.09 (failure)	52
SPB.2F1	4.68	2.34	0.5	12.5→	26.5
SPB.2F2		3.28	0.3	12.5→	35.6

Table 4. Description and values of ULS material safety factor coefficients

Description	Nomenclature	Value
Property source *Properties derived from experiments*	$\gamma_{m,1}$	1.15
Manufacturing process *Resin infusion, fully post-cured*	$\gamma_{m,2}$	1.20
Temperature *Experiment temperature 25-50°C, HDT* 55-80°C*	$\gamma_{m,3}$	1.20
Fatigue *Periodic inspection and maintenance, poor accessibility*	$\gamma_{m,4}$	2.00

Resin heat distortion temperature

Figures:
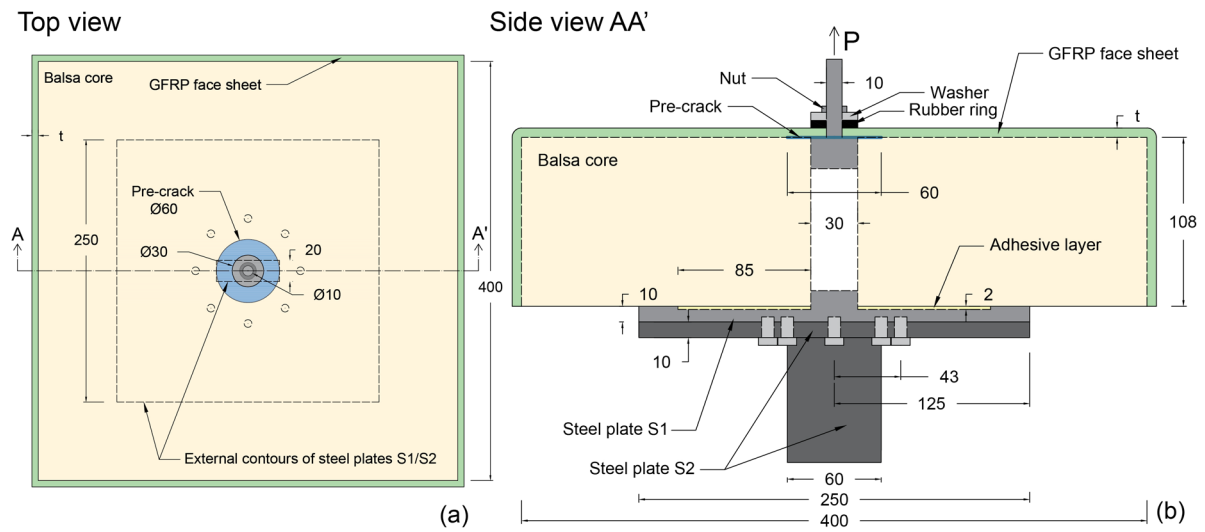
Fig. 1. Sandwich panel layout; (a) Top view and (b) Side view of section AA' in (a). Dimensions in mm
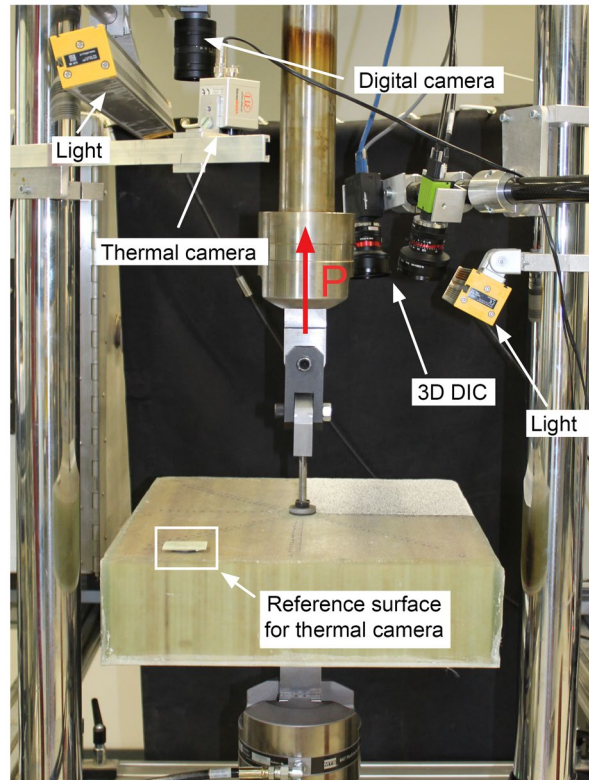
Fig. 2. Experimental set-up
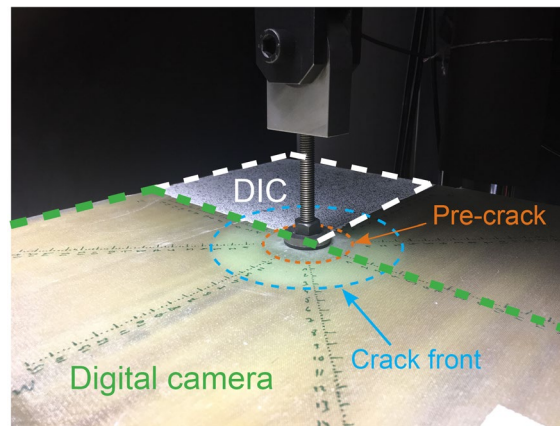
Fig. 3. Crack monitoring schema (common to all panels) and circular crack propagation pattern of sandwich panel SPA.1F
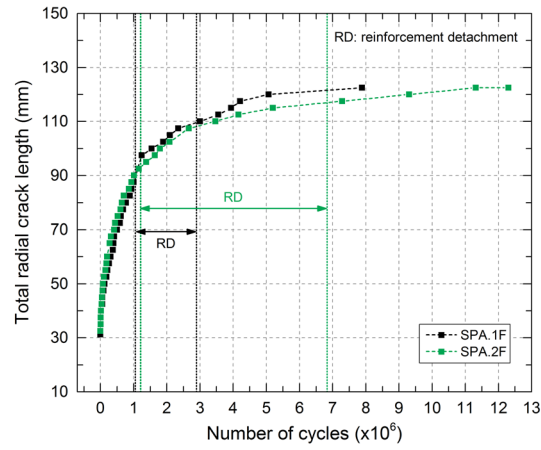
Fig. 4. Total radial crack length vs number of cycle curves of SPA configuration panels
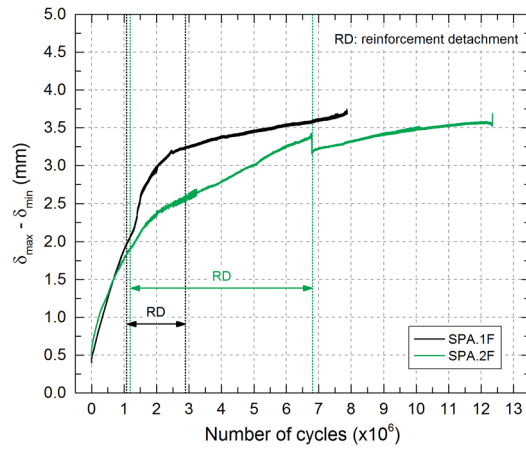
Fig. 5. Displacement increment vs number of cycle of SPA configuration panels
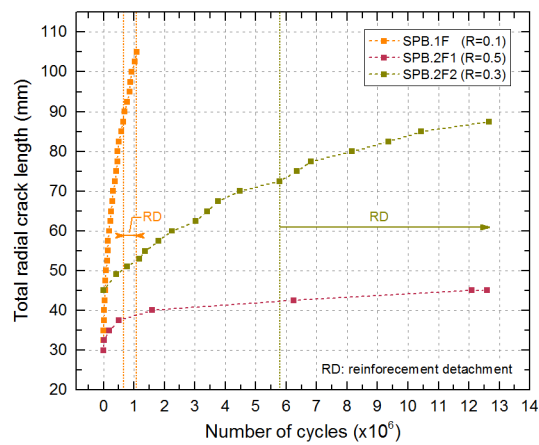
Fig. 6. Total radial crack length vs number of cycle curves of SPB configuration panels

25
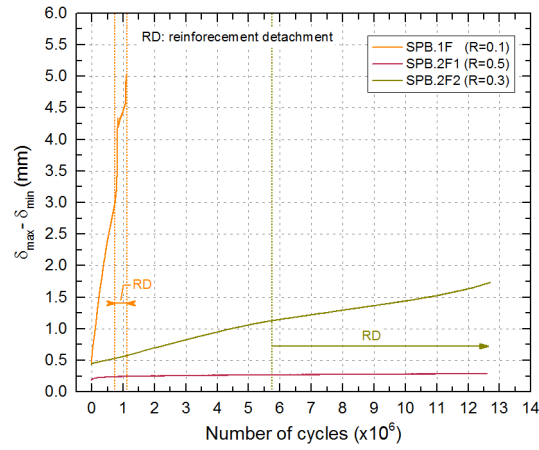
Fig. 7. Displacement increment vs number of cycle of SPB configuration panels
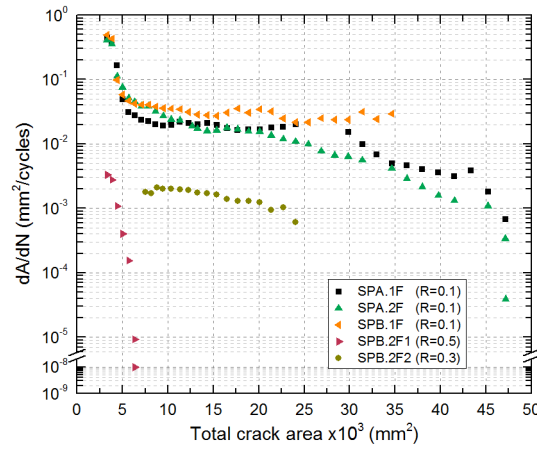
Fig. 8. Crack area growth rate vs total crack area
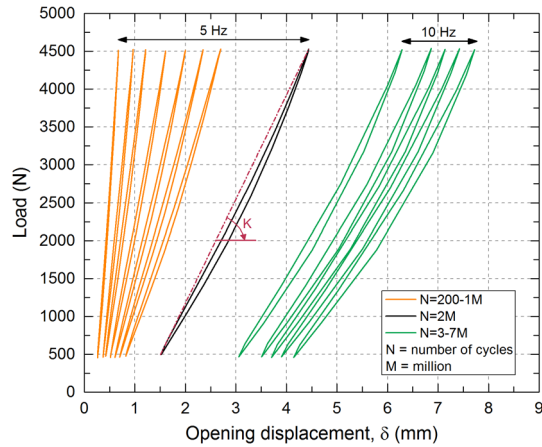
Fig. 9. Load-displacement hysteresis loops of SPA.1F panel
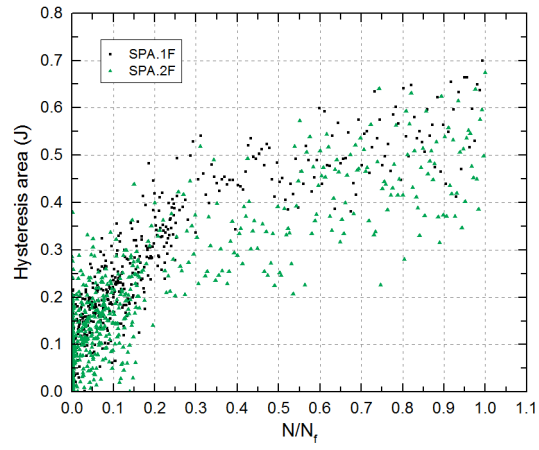
Fig. 10. Hysteresis area per cycle vs normalized number of cycles of SPA panels
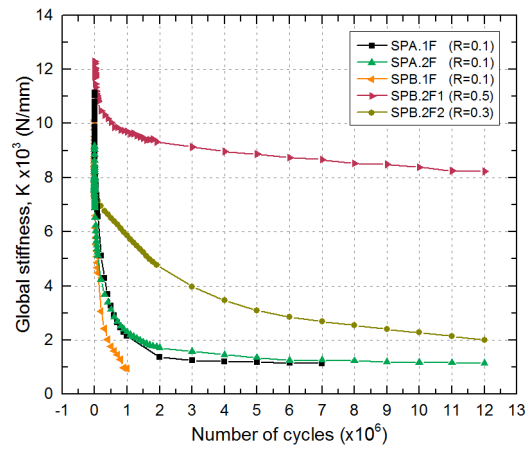
Fig. 11. Global stiffness vs number of cycles
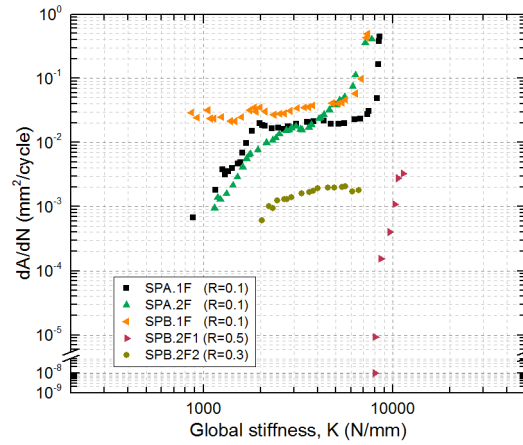
Fig. 12. Crack area growth rate vs global stiffness
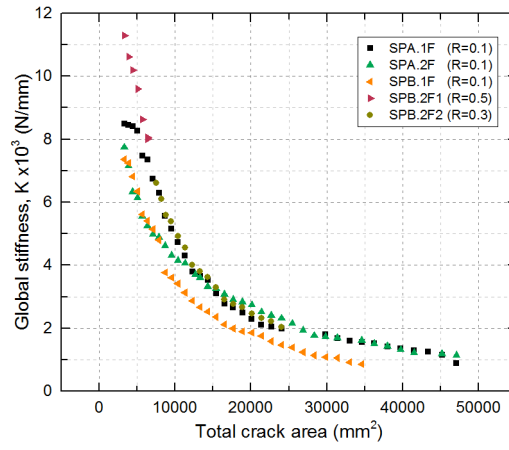
Fig. 13. Global stiffness vs total crack area
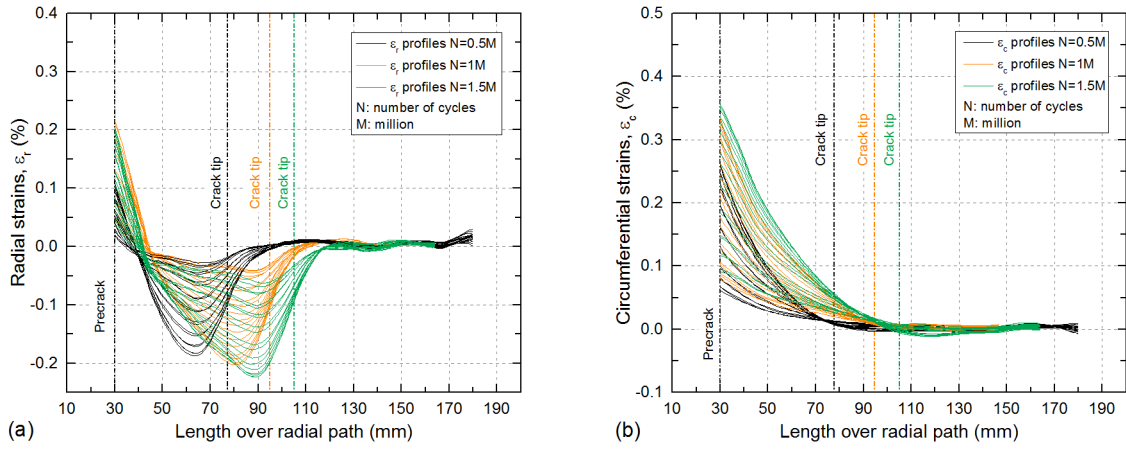
Fig. 14. Face sheet top surface in-plane strain distributions extracted from DIC; (a) in radial direction and (b) in circumferential direction for SPA.1F
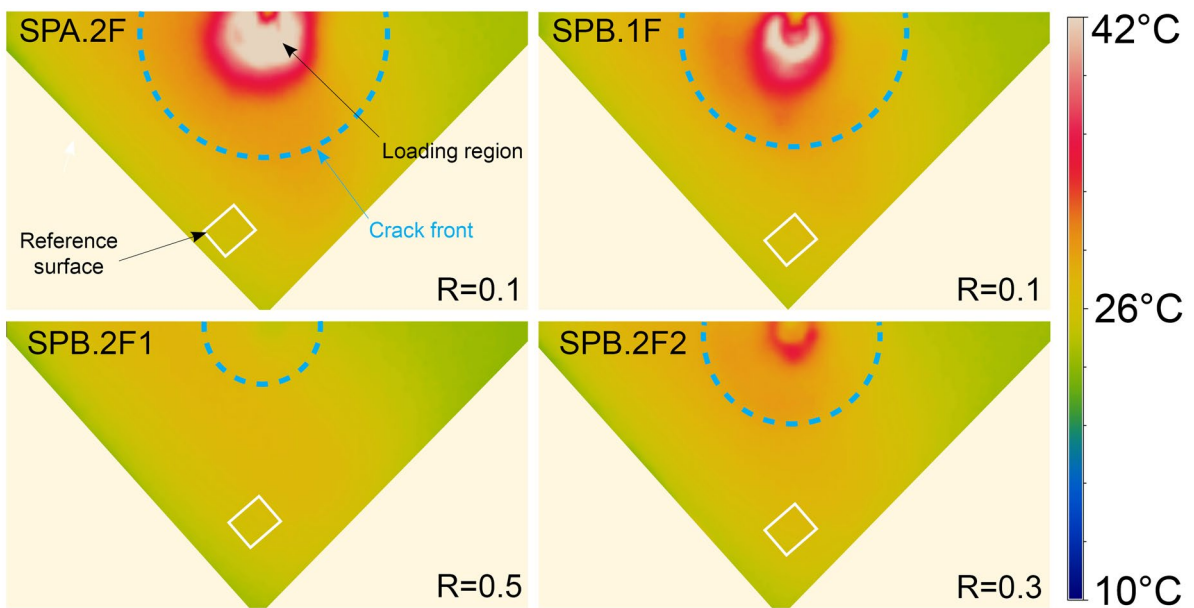
Fig. 15. Surface temperature before last fatigue cycles in four of performed experiments
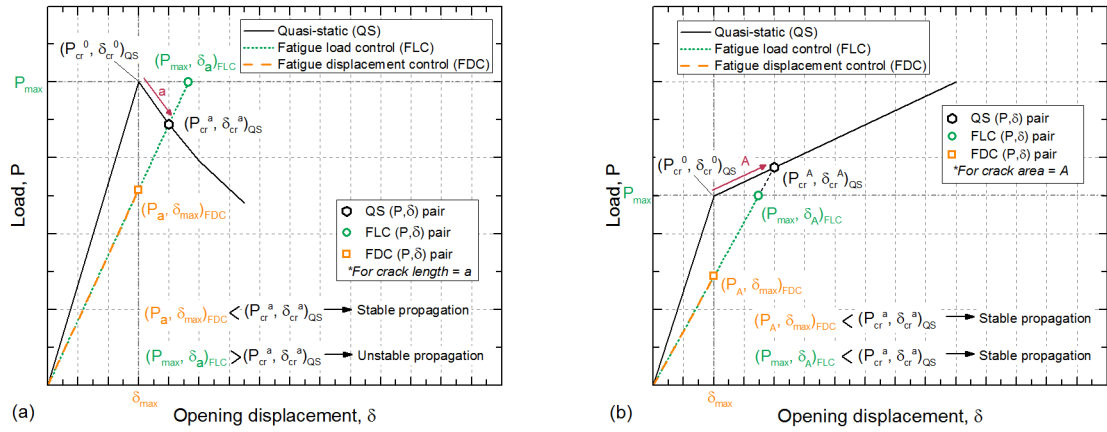
Fig. 16. Schematic comparison between load and displacement control in (a) 1D and (b) 2D fatigue fracture experiments
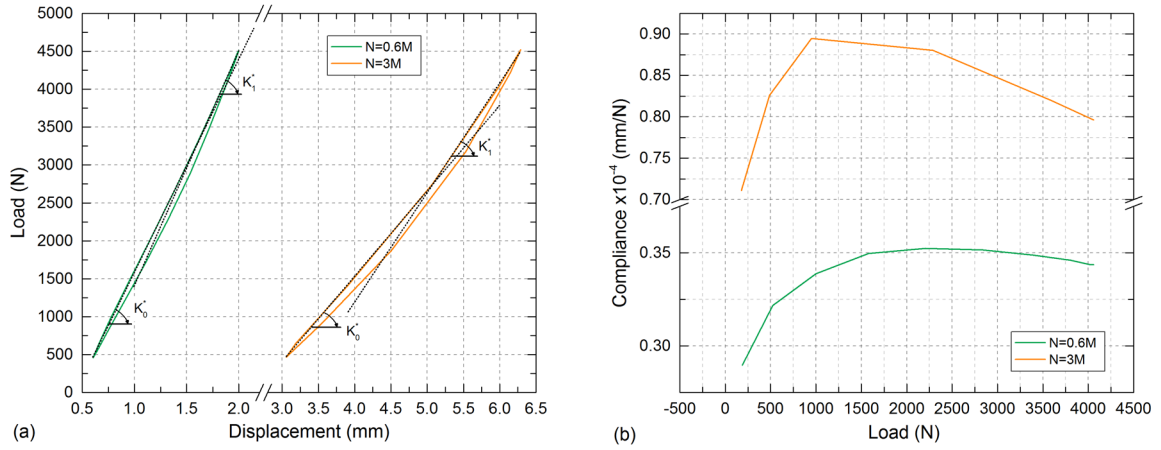

Fig. 17. (a) Load displacement hysteresis loops and (b) loading part compliances vs load curves at 0.6 million cycles and 3 million cycles; results for SPA.1F panel
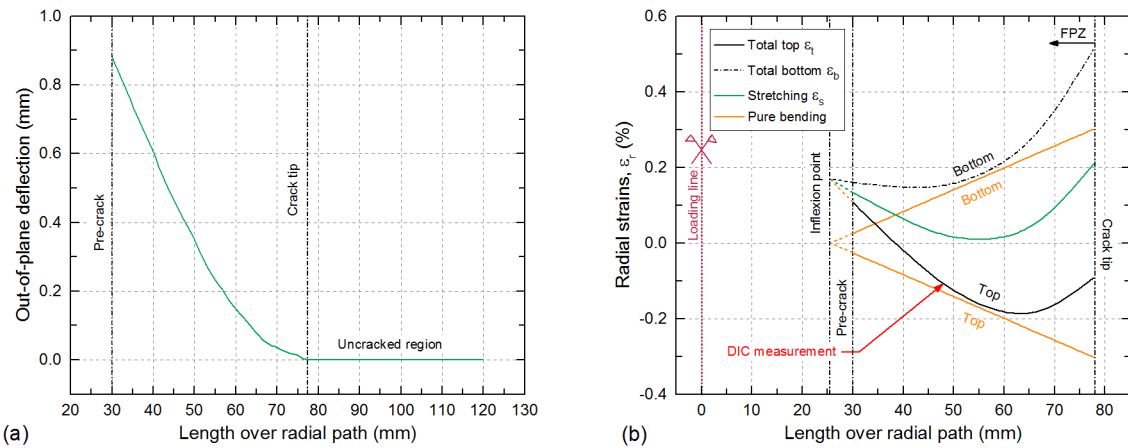

Fig. 18. Results obtained from face sheet top surface of panel SPA.1F at maximum deformation state at cycle 0.5M; (a) out-of-plane radial deflection profile; (b) radial strain profiles; all data derived from DIC
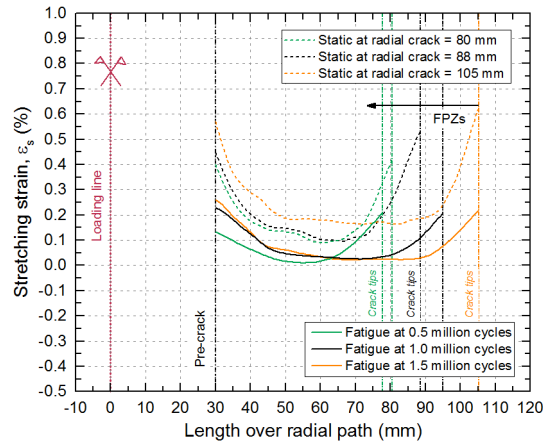
Fig. 19. Comparison of calculated radial stretching strains in fatigue SPA.1F and static SPA.2 [37] panels
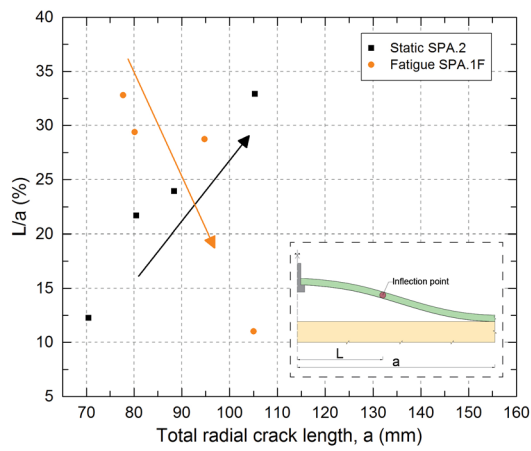

Fig. 20. Evolution of inflection point with crack propagation in fatigue SPA.1F and static SPA.2 [37] panels